ACS OMEGA

http://pubs.acs.org/journal/acsodf

Article

Nano-enhanced Dialytic Fluid Purification: CFD Modeling of Pb(II) Removal by Manganese Oxide

Kyriakos Atmatzidis, Farbod Alimohammadi, Nirupam Aich, and Rouzbeh Tehrani*

Cite This: *ACS Omega* 2020, 5, 32697−32705

Read Online

ACCESS | Metrics & More | Article Recommendations | Supporting Information

ABSTRACT: Nano-enhanced dialytic fluid purification is an evolution of biomedical dialysis that has been proposed as a novel method for applying nanomaterials in water treatment. Using nanosized hexagonal birnessite (δ-MnO_2) in a simplified dialytic system, we demonstrate herein an almost complete removal (98%) of Pb(II) within 3 h of treatment while monitoring environmental variables pH and Eh (redox potential). A mathematical model of the purification process is constructed in COMSOL Multiphysics to demonstrate how nanoadsorption using free-flowing nanoparticles in a dialytic system can be studied theoretically using computational fluid dynamics (CFD). The CFD model closely agrees with experimental results, estimating a 95% removal over 3 h of treatment and suggesting an 18% consumption of available adsorbent capacity. Additional insights into the progress and mechanisms of the adsorption process are also revealed. Finally, the nanoenhanced model is compared against standard dialysis absent of nanomaterials using COMSOL, and key differences in removal efficiency are highlighted. Results indicate that nanoenhanced dialysis can attain almost complete removal in 3 h of treatment or reach the same removal goal as standard dialysis in less than two-third of the treatment time.

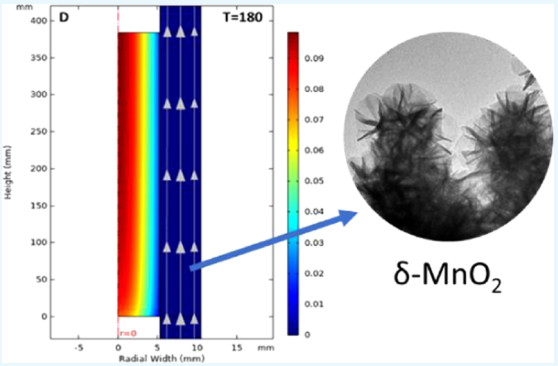

INTRODUCTION

In our previous work, we demonstrated how a simplified tubular dialytic system can employ a stream of suspended ferrihydrite nanoparticles to remove arsenite from an aqueous solution.[1] This treatment method, known as nanoenhanced dialytic fluid purification, was proposed as a novel alternative method for employing nanoadsorbents in water treatment. It eliminated the need for supporting media and maintained a continuous separation between the treated water and the nanoadsorbent fluid stream via a membrane barrier. The nanoenhanced dialytic system provided continuous, fast contaminant removal until the adsorbent was exhausted. Spent material could then be easily removed and replaced without requiring an additional separation mechanism and without disrupting the solution being treated. In essence, our demonstrated process was an evolution of dialysis used in biomedical applications and aimed to address the challenges of applying nanomaterials in water treatment using conventional methods.[2,3]

In this contribution, divalent lead (Pb(II)) was used as a model contaminant and hexagonal birnessite (δ-MnO_2) as a model nanoadsorbent to demonstrate the ability of nanomaterials to significantly enhance dialytic fluid purification. Environmental variables Eh (redox potential) and pH were also monitored. The use of divalent lead as a model contaminant was motivated following the recent exposure of Washington, DC and Flint, MI residents[4−7] to high levels of lead and lead's ability to cause serious health conditions.[8,9] In low ionic strength and slightly acidic aqueous conditions, lead is predominantly in its free divalent form.[9,10] Hexagonal birnessite (δ-MnO_2) was used as the model nanoadsorbent given its layered surface area, negative surface charge at circumneutral pH, and high adsorption capacity[11−13] that makes it a natural high affinity,[14] strong sorber[15] for divalent lead.

In addition, we developed a mathematical model using COMSOL Multiphysics to simulate the nanoenhanced removal process. For the first time, a method is described for representing nanoadsorption using free-flowing nanoparticles in computational fluid dynamics (CFD). The model is compared against the experimental results, and parameters of the purification process that were experimentally unexplored in our previous work are now investigated. The simulated nanoenhanced process is also compared with standard dialytic purification absent of nanomaterials using COMSOL. Key advantages in removal efficiency using the nanoenhanced dialysis process are highlighted and discussed.

Received: October 17, 2020
Accepted: December 1, 2020
Published: December 11, 2020

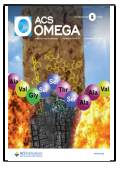

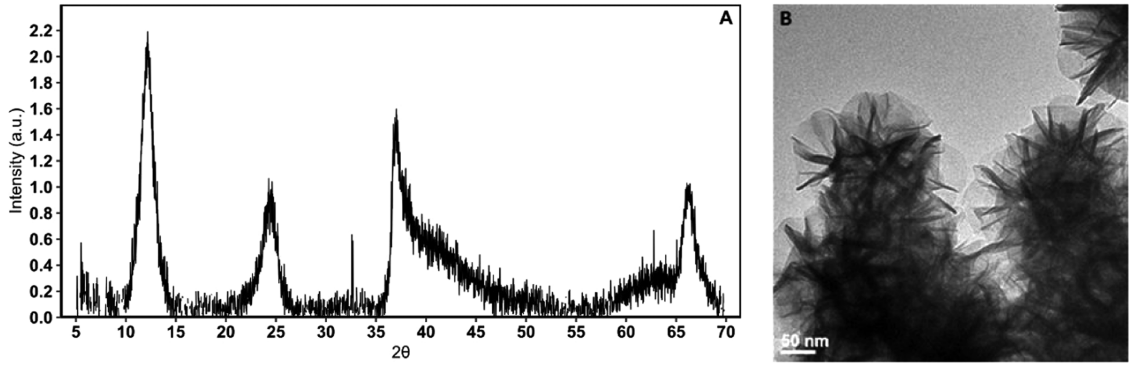

Figure 1. XRD diffractogram (A) and TEM image (B) of synthesized δ-MnO_2.

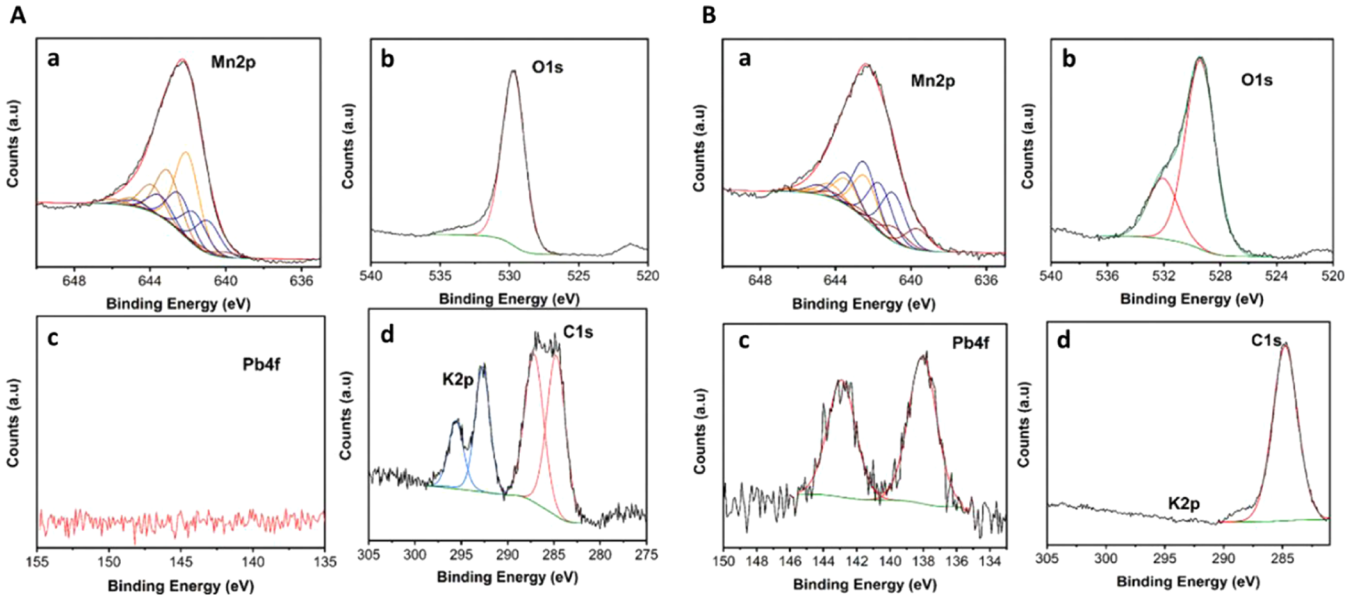

Figure 2. X-ray photoelectron spectroscopy (XPS) spectra of pristine synthesized birnessite (A) and used birnessite containing adsorbed lead and water in the interlayer space (B).

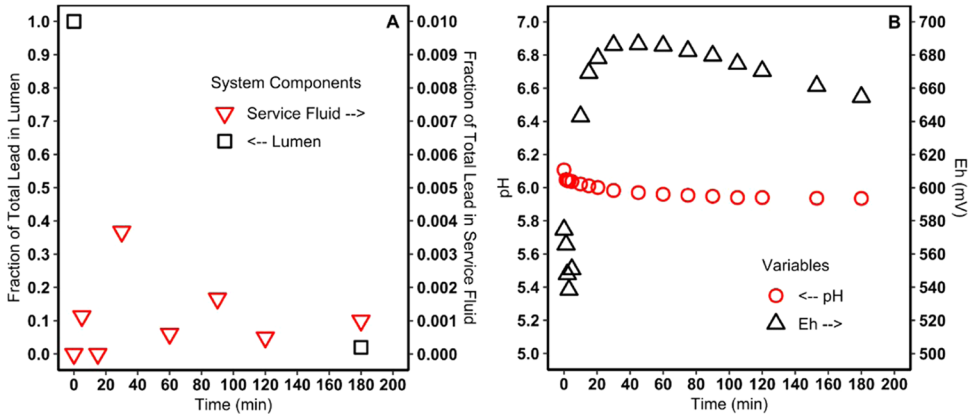

Figure 3. Removal of lead (A) and changes in pH and Eh (B) in the dialytic purification system.

RESULTS AND DISCUSSION

Characterization of Pristine and Used Birnessite (δ-MnO_2). *Crystal Structure and Morphology Analysis.* The X-ray diffractogram (XRD) in Figure 1A identifies the material as hexagonal birnessite. There are four major diffraction peaks identifiable at 2θ values of 12, 24, 37, and 66° that define the δ-phase of MnO_2 and are in good agreement with Bragg peak ranges reported throughout the literature for Cu Kα (λ = 1.54060 Å) irradiation: 12, 24−26, 36−38, and 65−67°. The peaks at 2θ values of 12 and 24° of the XRD pattern correspond to the (001) and (002) Bragg reflections and indicate the interlayer and half-interlayer spacing of birnessite at 7.3 and 3.7 Å, respectively. The additional diffraction peaks at 2θ values of 37 and 66° can be attributed to the (111) and

https://dx.doi.org/10.1021/acsomega.0c05069
ACS Omega 2020, 5, 32697−32705

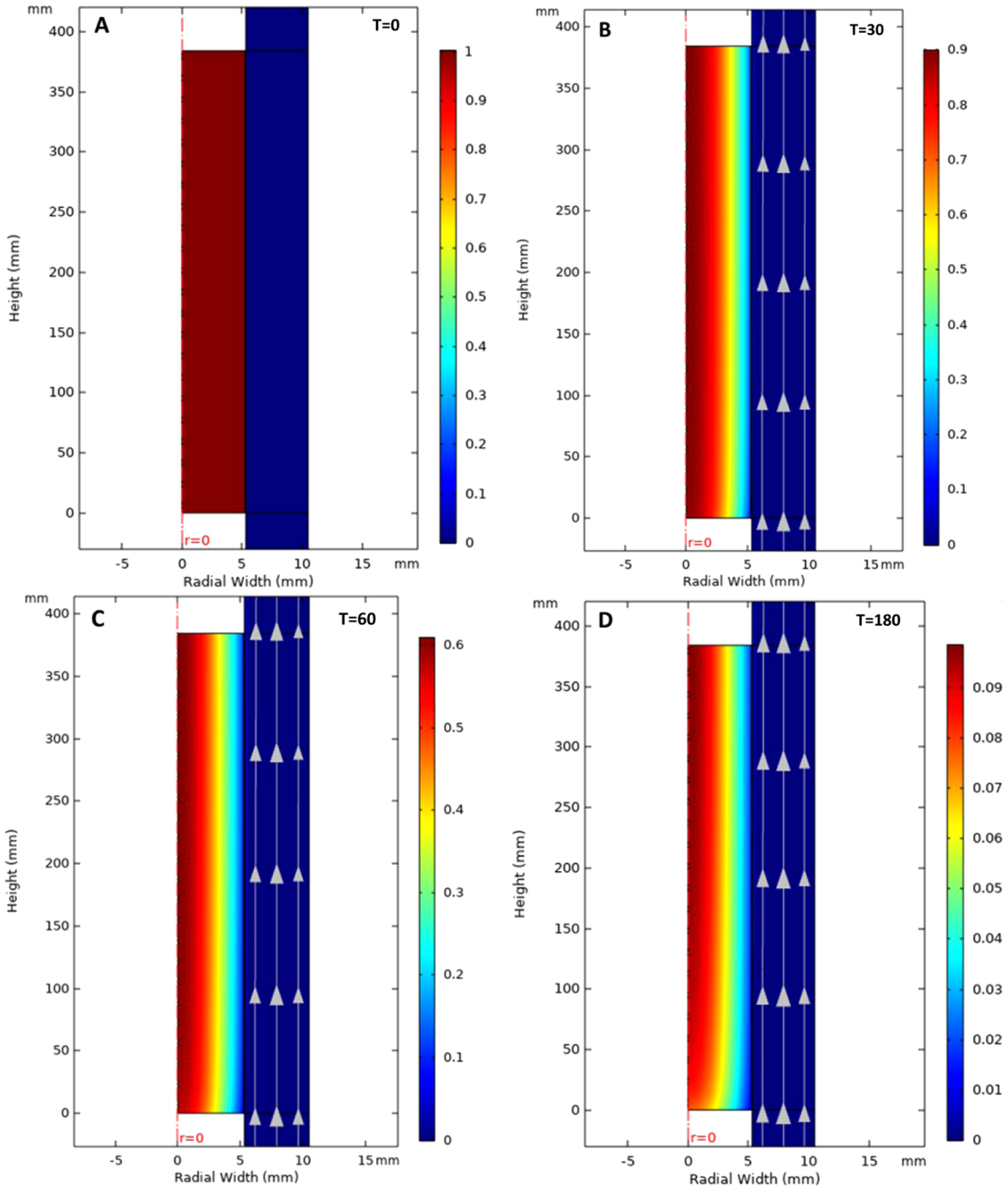

Figure 4. Surface plot of the Pb(II) concentration distribution in all domains of the purification system model at time T = 0 (A), 30 (B), 60 (C), and 180 (D) min of simulation. Concentrations of lead on the scale bars are presented as normalized values.

(020) planes.[16] A further peak may be found from 2θ values of 78−79° for extended scan ranges.[11,14,17−20] Figure 1B also shows nanoflower morphologies in aggregated particles indicative of the morphology of δ-phase MnO_2.[17]

Adsorption of Pb(II) onto Birnessite (δ-MnO_2). X-ray photoelectron spectroscopy (XPS) was used to verify the adsorption of Pb(II) to the birnessite interlayer. In Figure 2A, peaks at 642 and 530 eV indicate the presence of manganese (a) and oxygen (b) in the lattice of pristine MnO_2, respectively. Peaks at 293 and 296 eV in the spectrum (d) indicate intercalated potassium, while the absence of peaks in the spectrum (c) shows the absence of lead in unused birnessite. After the purification process, Figure 2B shows two new peaks in the spectrum (c) at 138 and 143 eV attributable to Pb $4f_{7/2}$ and Pb $4f_{5/2}$, respectively, and a new higher energy peak at 532 eV in spectrum (b) from H_2O, indicating the presence of lead and water in the interlayer space. Furthermore, the splitting of peaks in spectrum (a) of Figure 2B indicates that the average oxidation state of birnessite has decreased from 3.5 to 3.1. This is consistent with lead sorption to birnessite in prior studies.[21,22]

Dialytic System Performance. Performance of the nanoenhanced dialytic purification system was evaluated by tracking lead concentrations in both the lumen (LU) and the service fluid (SF) over time and by observing changes in the environmental variables pH and Eh. (Though not referenced as such in this work, solutions of the LU and SF are

https://dx.doi.org/10.1021/acsomega.0c05069
ACS Omega 2020, 5, 32697−32705

synonymous with the terms dialysate and permeate, respectively, in traditional dialysis).

In Figure 3A, the amount of lead in each component is presented as a mass fraction of the total lead added into the lumen initially (33.0 mg). This amount of lead in the lumen (965 mg/L) created a high concentration gradient within the dialytic system that could be monitored throughout the treatment duration. After treatment, lead in the lumen had decreased by 98.0%. Because the membrane was under pressure during treatment and frequent sampling of the high concentration, small lumen volume would have interfered with the adsorption results in the system, multiple points for Pb(II) removal over time were not obtainable and are not shown.

If the removal efficiency of the system is defined as the amount of lead adsorbed to δ-MnO_2, then it can be calculated according to eq 1.

$$RE_{sys} = \frac{M_o^{LU}V^{LU} - (M_f^{LU}V^{LU} + V_s\sum_{n=1}^{m-n\geq 1} M_n^{SF} + M_m^{SF}V_f^{SF})}{M_o^{LU}V^{LU}} \quad (1)$$

In eq 1, M and V represent the concentration of Pb(II) (mg/L) and the volume of solution (L) with respect to the component of the system indicated by the superscripts. Thus, $M_o^{LU}V^{LU}$ is the initial mass of lead in the lumen (total lead); $M_f^{LU}V^{LU}$ is the mass of lead in the lumen at the end of the experiment; $V_s\sum_{n=1}^{m-n\geq 1} M_n^{SF}$ is the mass of lead sampled from the SF during the runtime; $M_m^{SF}V_f^{SF}$ is the residual mass of lead in the SF at the end of the experiment; and m is the total number of samples. A 97.9% removal efficiency calculation indicates that almost all of the lead was adsorbed by δ-MnO_2, leaving 0.1% in the SF, which is about the average value observed across the runtime of the experiment. This indicates that lead diffusing through the membrane was quickly adsorbed, and no substantial amount of Pb(II) had accumulated in the SF across time. The general trend of values in the SF shows a small spike in the Pb(II) concentration (to about 0.4% of total lead) within 30 min followed by a gradual decrease and eventual plateau (to about 0.1% of total lead). This indicates a flood of lead into the SF early in the treatment process that likely overcame the rate of adsorption but was resolved over the duration of the treatment.

Changes in the pH of the system are shown in Figure 3B. Overall, the pH of the service solution did not decrease significantly over time due to the presence of the MES buffer. The pH dropped from 6.11 to 6.05 within a few minutes and slowly settled to 5.94 by the end. MES is a noncomplex forming Good's buffer compatible with Pb(II) and has a pK_a of 6.1.[23] Near its pK_a, the affinity of δ-MnO_2 for Pb(II) is maximized without causing precipitation. The pH is also buffered against the release of accumulated protons on the δ-MnO_2 surface[24,25] and from the acidity of the adsorption reaction.[11−13]

Changes in the Eh of the system are also shown in Figure 3B. In contrast to the pH, the redox potential (Eh) of the SF varied considerably. The introduction of δ-MnO_2 into the SF saw a sudden small drop of 36 mV within several minutes. A relatively fast increase of 148 mV was observed over 30 min followed by a smooth, slow decrease of 31 mV by the end of the experiment. Since the service solution pH was buffered, the observed Eh changes reflect changes in the composition of redox species in the solution due to adsorption. These are attributed to a fast adsorption uptake of lead and a slower equilibration process, respectively.

CFD Model Simulation Performance and Comparison to the Experimental System. Simulation of the nano-enhanced dialytic process and progress over time are shown in Figure 4 using two-dimensional (2D) surface plots. The concentrations of lead in the domains of the model have been normalized by the total amount of lead added into the system. At the start of the simulation ($T = 0$), all lead was contained in the lumen domain and the normalized concentration was unity. During simulated treatment, service fluid (SF) containing the δ-MnO_2 available sites (not shown) was continuously recirculated as indicated by the gray streamlines. Without mixing, a concentration gradient developed quickly within the lumen as Pb(II) most proximal to the membrane interface quickly diffused into the service solution first. The concentration gradient within the lumen decreased progressively over time thereafter as Pb(II) from the center of the lumen (near the axis of symmetry) diffused into the SF. The lower quarter of the lumen domain showed a higher reduction in Pb(II) than other areas due to hydrostatic pressure. Pb(II) that had diffused into the SF was quickly adsorbed, and Pb(II) is not observed in the dialyzer/SF domains at any time. According to the scale bar of Figure 4D, the majority of Pb(II) was removed from the lumen and no substantial amount accumulated in the SF by the end of the treatment duration.

Performance of the simulated Pb(II) removal is also shown using standard plots in Figure 5 for comparison to experimental results. The average concentrations of Pb(II) in

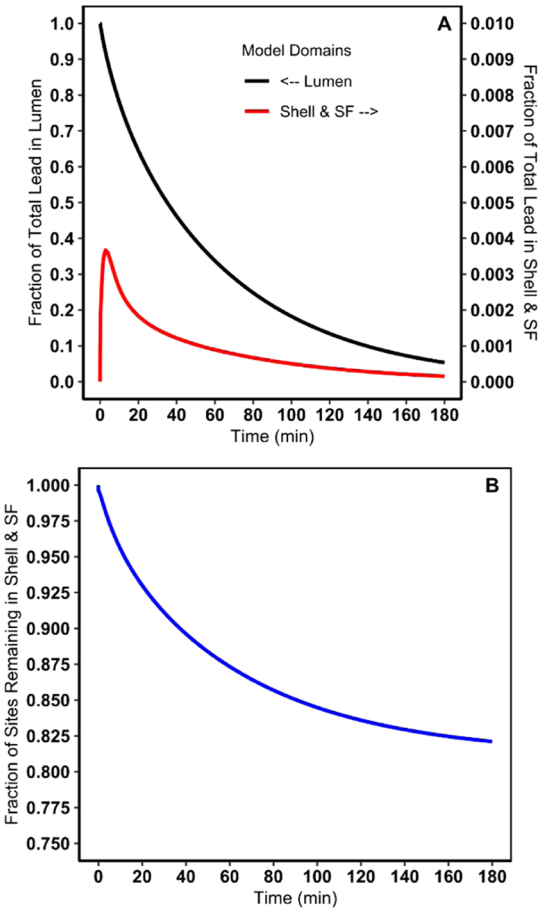

Figure 5. Removal of lead (A) and consumption of available δ-MnO_2 adsorption sites (B) in the model simulation of the purification system.

https://dx.doi.org/10.1021/acsomega.0c05069
ACS Omega 2020, 5, 32697−32705

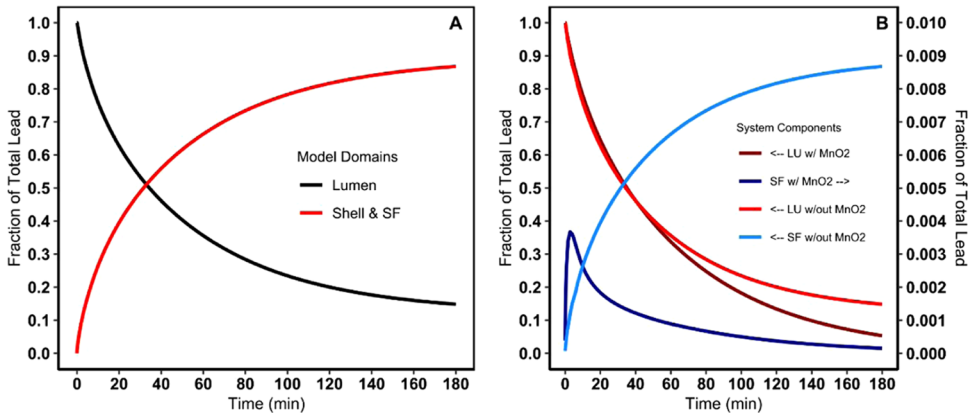

Figure 6. Simulation of Pb removal in the absence of δ-MnO_2 nanoparticles (A) and comparison of dialytic purification with and without the use of δ-MnO_2 nanoparticles (B) (see the Supporting Information for additional details).

both the lumen and the shell/SF domains were tracked over the runtime of the simulation and are both shown in Figure 5A.

Pb(II) concentration in the lumen showed a parabolic decline over the simulation runtime with a 95% removal, which is comparable but short of the system's 98% removal. According to Figure 5 only 18% of the available surface sites were consumed in the adsorption process and Pb(II) did not significantly accumulate in the shell/SF domains to affect the transmembrane concentration gradient. Therefore, the model's reduced removal may be related to the diffusion rate of Pb(II) throughout the lumen and membrane domains. The diffusion rate of Pb(II) in those regions is dependent on the accuracy of the diffusion coefficients used and on the absence of mixing that allows the concentration of the Pb(II) solution to stratify within the lumen. In the physical system, minor mixing is possible from the pulsating nature of the peristaltic pump that is challenging to represent in the model.

As seen in the experimental data, lead concentration in the SF of the simulation reached a maximum accumulation of 0.37%. This was constrained by design to match the highest value observed in the experimental system and to define $k_{f,min}$ (see the Chemistry section in the Computational Methods section). However, Figure 5A shows a trend for the concentration of Pb(II) in the SF akin to the one in Figure 3A. This was not predefined and shows an early spike of Pb(II) concentration in the SF followed by a gradual decrease and eventual plateau. The spike in this case was also likely due to a sharp increase in Pb(II) flux through the membrane that briefly overcame the rate of adsorption. The model peaked immediately after the start of the simulation when Pb(II) proximal to the membrane interface was the highest and rushed into the service fluid. This can be inferred visually by comparing Figure 4A at t = 0 min with Figure 4B at t = 30 min, where the concentration of lead in the lumen proximal to the membrane region is reduced suddenly from unity to approximately 0.3. This is a dramatic drop in comparison to the subsequent plots of Figure 4 where changes in lumen lead concentration near the membrane region are minimal. In contrast to the model, the experimental system peaked around 30 min, suggesting that the physical membrane may have delayed solute transport. Nonetheless, there is good agreement in the removal of lead between the experiment and the simulation over 3 h of nanoenhanced dialysis.

The advantage of nanoenhanced dialysis is clearly evident when compared to the effectiveness of standard dialysis. Figure 6A shows that standard dialysis can remove lead from the lumen only to the extent that Pb(II) can diffuse throughout the entire volume of the system and reach an equilibrium concentration. By dilution alone, the system can reduce the concentration of lead within the lumen by an asymptotic maximum of 88% at infinite runtime. In contrast, nanoenhanced dialysis can reach for almost complete removal within 3 h, as shown in Figure 3A (experimental, 98%) and Figure 5A (simulated, 95%). δ-MnO_2 nanoparticles act as a continual sink for lead, minimizing accumulation in the SF and maintaining a continuous transmembrane concentration gradient. As a result, Pb(II) continuously diffuses, though at diminishing rates over time, from the membrane until almost all of it is removed. Furthermore, Figure 6B combines Figures 5A and 6A to elucidate another advantage offered by nanoenhanced dialysis. According to the graph, the maximum removal of lead (88%) for standard dialysis is attained at 180 min. In contrast, the same removal goal for nanoenhanced dialysis is attained at approximately 115 min. The result suggests that nanoenhanced dialysis can offer a substantial reduction in treatment time, over 60 min or >33% in this case, and can have profound implications for time-sensitive fluid purification processes.

CONCLUSIONS AND FUTURE WORK

Using divalent lead (Pb(II)) as a model contaminant and hexagonal birnessite (δ-MnO_2) as a model nanoadsorbent, we have demonstrated the ability of nanomaterials to significantly enhance dialytic fluid purification and have highlighted its advantages over standard dialysis. Experimentally, a 98% removal of Pb(II) was attained under stable pH and shifting Eh conditions with no significant accumulation of Pb(II) in the service fluid (SF). A model of our dialytic system was created in COMSOL Multiphysics highlighting in detail the underlying considerations for representing free-flowing nanoparticles in CFD simulations. Time-dependent simulations of the experimental system predicted a 95% removal of Pb(II), no significant accumulation of Pb(II) in the SF, and an 18% consumption of δ-MnO_2 adsorption capacity. Simulated results were in close agreement with experimental results, demonstrating the utility of the model. Simulations contrasting nanoenhanced dialysis with standard dialysis also suggested that the former can offer improved removal within an

https://dx.doi.org/10.1021/acsomega.0c05069
ACS Omega 2020, 5, 32697−32705

equivalent treatment duration or reduced treatment duration for an equivalent removal goal over the latter.

The CFD model that has been developed provides an initial template for describing nanoenhanced dialysis computationally, and future work should focus on addressing some current limitations. For example, the remaining adsorption capacity reported did not account for loss due to aggregation, and future models should incorporate this phenomenon. Furthermore, a theoretical description of the time-dependent kinetics of dialysis should be developed to avoid the semiempirical dependence of future models. A complete description of nanomaterial dynamics in nanoenhanced dialysis would be a significant milestone in adopting the use of this fluid purification process. It would also foster the development of other fluid processes incorporating nanoadsorption by providing a theoretical basis for initial studies using CFD.

EXPERIMENTAL SECTION

Synthesis and Characterization of Birnessite (δ-MnO_2). Hexagonal birnessite (δ-MnO_2) was synthesized by an adaptation of the McKenzie procedure. Briefly, $KMnO_4$ solution (0.4 M, 250 mL) was heated at 80 °C and hydrochloric acid (HCl, 4 M, 50 mL) was added dropwise (1 mL/min) for 30 min. The mixture was aged for 15 h at 50 °C, centrifuged, and washed five times with distilled water before air drying.[26]

X-ray diffractograms of synthesized birnessite were obtained using a Bruker D8 ADVANCE diffractometer operating at 40 kV and 40 mA using Cu Kα radiation (λ = 1.5406). The powder samples were scanned from 2θ values of 5 to 70°. Tunneling electron microscopy (TEM) micrographs were taken using a JEOL JEM-1400 microscope.

X-ray photoelectron spectroscopy (XPS) spectra of birnessite before and after lead adsorption were collected using a homemade instrument with a Cu Kα source.

Dialytic System Experiment. Component layout and assembly of the dialysis system have been outlined in our previous work.[1] Briefly, a tubular, single-membrane (cellulose acetate, 100 kDa) dialyzer (Figure 7) was fixed on a ring stand

Figure 7. Sketch of the dialyzer used in experimental nanoenhanced dialysis containing δ-MnO_2 nanoparticles in the shell region.

and attached in a closed circuit via C-flex tubing to a peristaltic pump and a stirred beaker solution. Redox and pH probes were fixed from the ring stand into the beaker mixture. In preparation for use, the dialyzer membrane was primed using a 15 min rinse of 10% ethanol followed by several rinses of deionized water.

To start the nanoenhanced purification process, 34.2 mL of pH 4.0 Pb(II) solution, prepared from 99.99% pure Acros Organics $Pb(NO_3)_2$, was added by hand into the lumen of the membrane. A sample from the excess of this solution was preserved with concentrated nitric acid and later analyzed to determine the initial total lead concentration. Then, a 250 mL of service solution containing 9.2 mM of 2-(*N*-morpholino)-ethanesulfonic acid (MES) was added into the beaker and set to a pH of 6.1 using 1 M HNO_3. An initial 5 mL of the sample was taken from the beaker, and δ-MnO_2 was added to attain a loading of 1.20 g/L. The service solution was continuously stirred and pumped throughout the system at a volumetric flow rate of 350 mL/min. Over the course of 3 h, 5 mL samples were taken from the beaker, filtered through a 0.45 μm PTFE syringe filter, acidified with concentrated nitric acid to a pH below 2, and refrigerated for preservation. Changes in pH and Eh of the service fluid (SF) were also tracked over the runtime of each experiment. At the end of the experiment, a final sample was taken from the lumen of the membrane. All samples were analyzed for lead concentration using a Thermo Scientific iCAP Q inductively coupled plasma mass spectrometer (ICP-MS) operated by Alpha Analytical, Inc. following EPA Method 200.8 for total lead analysis. The membrane lumen solution had an initial lead concentration of 965 mg/L (or 33.0 mg of total lead).

Computational Methods. *Construction of the CFD Model for Nanoenhanced Dialytic Purification.* A mathematical model for the nanoenhanced dialysis system was developed in COMSOL Multiphysics 5.5 using the computational fluid dynamics (CFD) module. A simplified geometry of the dialysis system was created, physics relevant to the purification process were assigned, and the process was simulated over the same runtime as the experiment.

The following assumptions were considered in the model development:

- The solution within the lumen is stagnant and does not mix.
- Pb(II) species do not concentrate and polarize at the lumen−membrane interface.
- δ-MnO_2 nanoparticles do not readily diffuse into the membrane lumen.
- δ-MnO_2 nanoparticles are homogeneous, uniformly distributed, and do not aggregate in the SF.
- Fluid flow is incompressible and Newtonian, and the low concentration of δ-MnO_2 nanoparticles in the SF does not significantly affect fluid properties.

Geometry Creation. Taking advantage of the dialyzer's symmetric cylindrical form and to minimize computational cost, the system was modeled using a simplified 2D axisymmetric geometry with coordinates r and z. Figure 8 shows five rectangular domains organized about a vertical axis of symmetry (r = 0) in 2D space that represent the various components of the system. The lumen and shell domains, containing the membrane domain between them (not labeled), comprise the dialyzer tube. Table S1 lists the dimensions of these domains obtained from the physical measurements of the dialyzer. The last two domains, extending above and below the shell domain, together represent contributions from the beaker and tubing. In this case, the real geometry of these components was adapted to compliment the 2D geometry of the dialyzer. Each extension was sized to contain half the remaining volume of the SF not contained within the dialyzer shell and to interface directly with the dialyzer shell domain. Dimensions of these domains are provided in Table S1 but are not physical.

https://dx.doi.org/10.1021/acsomega.0c05069
ACS Omega 2020, 5, 32697−32705

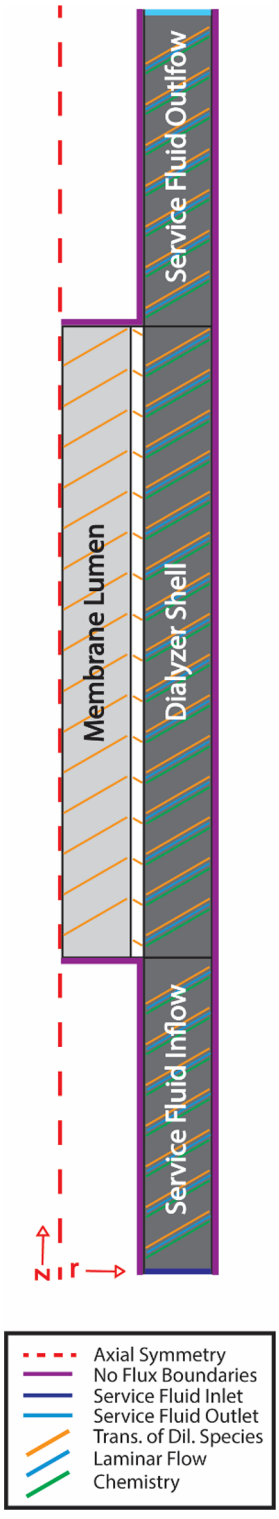

Figure 8. Two-dimensional geometry of a dialyzer and configuration of physics in COMSOL (figure not to scale).

This was a reasonable adaptation when viewing the dialyzer as the central component of the system circuit, where SF originates from and returns to the stirred beaker. In this approach, the function of the stirred beaker, which maintains suspension of the nanomaterial and homogeneity of the SF, was conserved by specifying appropriate conditions at the fluid inlet and outlet boundaries.

Assignment of Physics & Definition of Model Parameters. The purification process involves the continuous diffusion of Pb(II) from the lumen into the dialyzer shell to be adsorbed by flowing δ-MnO_2 nanoparticles. For the simulation in COMSOL, this process was separated into individual "physics," transport of diluted species (TDS), single-phase flow (SPF), and chemistry (CHEM), driven by fundamental equations and solved concurrently within their specified domains. Figure 8 shows the pertinent physics in each domain of the geometry.

Treatment of Diluted Species (TDS). TDS describes the transient concentration distributions of Pb(II) and δ-MnO_2 (available vacant sites) throughout the geometry according to the advection−diffusion−reaction eq 2.

$$\frac{\partial C_i}{\partial t} = -u\cdot\nabla C_i + D_i(\nabla^2 C_i) + R_i \tag{2}$$

In eq 2, C_i and D_i are the concentration and diffusion coefficient of a species i (Pb(II) or δ-MnO_2 sites), respectively, u is the fluid velocity, and R_i is the adsorption reaction rate. TDS applied in all domains within the bounds of the geometry, but the mechanism of transport differed between domains. Within the lumen and membrane domains where the Pb(II) solution is stagnant, there was no fluid convection but only diffusion of Pb(II) through the membrane. Experimental results (not shown) suggest that δ-MnO_2 does not readily pass into the lumen and was therefore restricted from diffusing into the membrane/lumen in the model. In the shell and SF domains, both diffusion and convection contributed to species transport due to fluid flow, and species were also consumed from the adsorption reaction. Values for the diffusion coefficients of Pb(II) and δ-MnO_2 in each domain were estimated or derived from the literature and are provided in Table S2.

Single-Phase Flow (SPF). SPF describes fluid flow in the shell and SF domains according to the Naiver−Stokes equation for incompressible laminar flow (eq 3) (see the Supporting Information) and the continuity equation (eq 4).

$$\rho\left(\frac{\partial u}{\partial t} + u\cdot\nabla u\right) = -\nabla p + \mu\nabla^2 u + \rho g \tag{3}$$

$$\nabla\cdot u = 0 \tag{4}$$

In eqs 3 and 4, u is the SF fluid velocity, p is the pressure, ρ is the SF fluid density, μ is the SF fluid dynamic viscosity, and g is the acceleration due to gravity. A fully developed flow originated at the inlet of the SF inflow domain and ended at the outlet of the SF outflow domain. To maintain flow continuity and conservation of species, boundary conditions were prescribed to return the concentration of outflowing species at the outlet to the inlet at each time step t according to eq 5.

$$[C_{i,\,\mathrm{outlet}}]_t = [C_{i,\,\mathrm{inlet}}]_t \tag{5}$$

The concentration of species is returned to the inlet as a homogeneous distribution, emulating the function of the stirred beaker. The fluid velocity u remained constant across time, and atmospheric pressure was specified at the outlet. Because of a relatively low δ-MnO_2 loading in the SF, μ and ρ of the SF fluid were based on the properties of water at room temperature.[27] Values for these parameters are provided in Table S3.

https://dx.doi.org/10.1021/acsomega.0c05069
ACS Omega 2020, 5, 32697−32705

Chemistry (CHEM). CHEM describes the adsorption of Pb(II) by δ-MnO_2 in the shell and SF domains using an adsorption reaction model. This model is based on the chemical reaction kinetics of bulk species in solution and follows a reaction rate law.[28] To develop a rate law for the adsorption process, the reaction was modeled using Langmuir kinetics;[11,14,29] several studies suggest that Pb(II)—δ-MnO_2 adsorption data fit well to the Langmuir isotherm. In this approach, adsorption was considered as a reversible, bimolecular elementary reaction between two bulk species in a solution: Pb(II) cations (M) and δ-MnO_2 available vacant sites (S) as shown in eq 6.[30]

$$M + S \rightleftharpoons MS \tag{6}$$

The initial concentration of Pb(II) (M_0) needed to define the reaction was determined experimentally using ICP-MS. The initial concentration of available vacant sites of δ-MnO_2 (S_0) was estimated using eq 7 following Azizian's expression for β in describing adsorption kinetics.[30] Equation 7 is dependent on the initial loading of δ-MnO_2 (g/L) into the SF (A_0) and on the intrinsic properties of δ-MnO_2: its molecular weight (MW_A) and its Langmuir adsorption capacity (q_e) for the specified solution conditions. Values for these parameters are provided in Table S4.

$$S_0 = \frac{A_0}{MW_A} \cdot q_e \tag{7}$$

The differential rate law for reaction (6) is shown in eq 8 and expresses the overall time-dependent rate of reaction (or rate of consumption, $R_{i,t}$) for both species (M and S) according to their time-dependent concentrations ($[M]_t^{SF}$ and $[S]_t^{SF}$) in the SF and the rate constants for adsorption (product formation, k_a) and desorption (reactant formation, k_d).

$$-\frac{d[M]_t^{SF}}{dt} = -\frac{d[S]_t^{SF}}{dt} = R_{i,t} = k_a[M]_t^{SF}[S]_t^{SF} - k_d[MS]_t^{SF} \tag{8}$$

At equilibrium, the Langmuir constant K_L can be used to determine the ratio between the adsorption and desorption rate constants k_a and k_d. However, because K_L is not a unitless equilibrium constant, it was converted to a true thermodynamic constant K_{eq} using eq 9.[31]

$$K_{eq} = \frac{k_a}{k_d} = K_L \cdot A_0 \cdot 10^3 \cdot 55.5 \tag{9}$$

Conversion of K_L data from Zhang,[14] Xu,[11] and Zou[29] to K_{eq} (Table S5) suggests that the adsorption of Pb(II) to δ-MnO_2 is significantly favored over desorption, and eq 8 can be reasonably approximated as eq 10 so long as $[S]_t^{SF} \gg [MS]_t^{SF}$.

$$R_{i,t} \cong k_f[M]_t^{SF}[S]_t^{SF} \tag{10}$$

In eq 10, k_f is the effective forward reaction rate constant. Because utilizing reaction rate constants obtained from conventional batch adsorption kinetic models may not be applicable for transient dialysis processes (see the Supporting Information), a parametric sweep was used to determine a minimum rate constant ($k_{f,min}$) according to eq 11.

$$R_{i,t} \geq k_{f,min}[M]_t^{SF}[S]_t^{SF} \tag{11}$$

The minimum value for the rate constant was chosen to limit the accumulation of Pb(II) in the SF to the maximum value observed in the experiment across time. This value is listed in Table S4.

Model Runtime (Study). To simulate the transient purification process, a time-dependent study was chosen for the model with a 180 min runtime using single-minute time steps. Average concentrations of Pb(II) and δ-MnO_2 were tracked in the lumen and dialyzer/SF domains to evaluate the extent of Pb(II) removal from the lumen, monitor the accumulation of Pb(II) in the SF, and determine the consumption of available δ-MnO_2 sites. The resultant plots were compared to experimental results for model validation.

Comparison of Nanoenhanced Dialysis with Standard Dialysis. Standard dialysis was conducted using the same COMSOL model outlined above including the same model geometry, physics, and boundary conditions. Only the adsorption reaction kinetics were disabled, and the fluid flow model was adjusted (see the Supporting Information for additional details).

■ ASSOCIATED CONTENT

Supporting Information

The Supporting Information is available free of charge at https://pubs.acs.org/doi/10.1021/acsomega.0c05069.

CFD model tables of values and parameter derivation, Reynolds flow regime for SF in COMSOL model, application of batch reaction kinetics in transient dialysis adsorption, application of the PSO model for transient dialysis adsorption, and computation of standard dialytic purification using COMSOL (PDF)

■ AUTHOR INFORMATION

Corresponding Author

Rouzbeh Tehrani − *Department of Civil and Environmental Engineering, Temple University, Philadelphia, Pennsylvania 19122, United States;* orcid.org/0000-0002-5989-7049; Email: r.tehrani@temple.edu

Authors

Kyriakos Atmatzidis − *Department of Civil and Environmental Engineering, Temple University, Philadelphia, Pennsylvania 19122, United States*

Farbod Alimohammadi − *Department of Chemistry, Temple University, Philadelphia, Pennsylvania 19122, United States;* orcid.org/0000-0002-5143-2933

Nirupam Aich − *Department of Civil, Structural and Environmental Engineering, University at Buffalo, Buffalo, New York 14260, United States;* orcid.org/0000-0003-1896-8127

Complete contact information is available at: https://pubs.acs.org/10.1021/acsomega.0c05069

Notes

The authors declare no competing financial interest.

■ ACKNOWLEDGMENTS

We thank Temple University's College of Engineering for supporting this work. We also thank Dr. Daniel R. Strongin, Department Chair of Chemistry at Temple University, for his review and suggestions in improving this manuscript.

REFERENCES

(1) Atmatzidis, K.; Alimohammadi, F.; Strongin, D. R.; Tehrani, R. Biomimetic System for the Application of Nanomaterials in Fluid Purification: Removal of Arsenic with Ferrihydrite. *ACS Omega* **2020**, *5*, 5873−5880.

(2) Santhosh, C.; Velmurugan, V.; Jacob, G.; Jeong, S. K.; Grace, A. N.; Bhatnagar, A. Role of Nanomaterials in Water Treatment Applications: A Review. *Chem. Eng. J.* **2016**, *306*, 1116−1137.

(3) Westerhoff, P.; Alvarez, P.; Li, Q.; Gardea-Torresdey, J.; Zimmerman, J. Overcoming Implementation Barriers for Nanotechnology in Drinking Water Treatment. *Environ. Sci. Nano* **2016**, *3*, 1225−1522.

(4) Pieper, K. J.; Martin, R.; Tang, M.; Walters, L.; Parks, J.; Roy, S.; Devine, C.; Edwards, M. A. Evaluating Water Lead Levels during the Flint Water Crisis. *Environ. Sci. Technol.* **2018**, *52*, 8124−8132.

(5) Pieper, K. J.; Tang, M.; Edwards, M. A. Flint Water Crisis Caused By Interrupted Corrosion Control: Investigating 'Ground Zero' Home. *Environ. Sci. Technol.* **2017**, *51*, 2007−2014.

(6) Edwards, M.; Triantafyllidou, S.; Best, D. Elevated Blood Lead in Young Children Due to Lead-Contaminated Drinking Water: Washington, DC, 2001-2004. *Environ. Sci. Technol.* **2009**, *43*, 1618−1623.

(7) Roy, S.; Edwards, M. A. Preventing Another Lead (Pb) in Drinking Water Crisis: Lessons from the Washington D.C. and Flint MI Contamination Events. *Curr. Opin. Environ. Sci. Heal.* **2019**, *7*, 34−44.

(8) Mushak, P.; Davis, J. M.; Crocetti, A. F.; Grant, L. D. Prenatal and Postnatal Effects of Low-Level Lead Exposure: Integrated Summary of a Report to the U.S. Congress on Childhood Lead Poisoning. *Environ. Res.* **1989**, *50*, 11−36.

(9) Hem, J. D. Inorganic Chemistry of Lead in Water. Lead in the Environment: GeologicalSurvey Professional Paper 957, 1976.

(10) Wang, X.; Wang, L.; Wang, Y.; Tan, R.; Ke, X.; Zhou, X.; Geng, J.; Hou, H.; Zhou, M. Calcium Sulfate Hemihydrate Whiskers Obtained from Flue Gas Desulfurization Gypsum and Used for the Adsorption Removal of Lead. *Crystals* **2017**, *7*, 270.

(11) Xu, M.; Wang, H.; Lei, D.; Qu, D.; Zhai, Y.; Wang, Y. Removal of Pb(II) from Aaqueous Solution by Hydrous Manganese Dioxide: Adsorption Behavior and Mechanism. *J. Environ. Sci.* **2013**, *25*, 479−486.

(12) Su, Q.; Pan, B.; Wan, S.; Zhang, W.; Lv, L. Use of Hydrous Manganese Dioxide as a Potential Sorbent for Selective Removal of Lead, Cadmium, and Zinc Ions from Water. *J. Colloid Interface Sci.* **2010**, *349*, 607−612.

(13) Qin, Q.; Wang, Q.; Fu, D.; Ma, J. An Efficient Approach for Pb(II) and Cd(II) Removal Using Manganese Dioxide Formed in Situ. *Chem. Eng. J.* **2011**, *172*, 68−74.

(14) Zhang, H.; Wu, A.; Fu, H.; Zhang, L.; Liu, H.; Zheng, S.; Wan, H.; Xu, Z. Efficient Removal of Pb(II) Ions Using Manganese Oxides: The Role of Crystal Structure. *RSC Adv.* **2017**, *7*, 41228−41240.

(15) Kwon, K. D.; Refson, K.; Sposito, G. Surface Complexation of Pb(II) by Hexagonal Birnessite Nanoparticles. *Geochim. Cosmochim. Acta* **2010**, *74*, 6731−6740.

(16) Zhu, S.; Huo, W.; Liu, X.; Zhang, Y. Birnessite Based Nanostructures for Supercapacitors: Challenges, Strategies and Prospects. *Nanoscale Adv.* **2020**, *2*, 37−54.

(17) Devaraj, S.; Munichandraiah, N. Effect of Crystallographic Structure of MnO2 on Its Electrochemical Capacitance Properties. *J. Phys. Chem. C* **2008**, *112*, 4406−4417.

(18) Musil, M.; Choi, B.; Tsutsumi, A. Morphology and Electrochemical Properties of α-, β-, γ-, and δ-MnO 2 Synthesized by Redox Method. *J. Electrochem. Soc.* **2015**, *162*, A2058−A2065.

(19) Della Puppa, L.; Komárek, M.; Bordas, F.; Bollinger, J. C.; Joussein, E. Adsorption of Copper, Cadmium, Lead and Zinc onto a Synthetic Manganese Oxide. *J. Colloid Interface Sci.* **2013**, *399*, 99−106.

(20) Liu, Z.; Xu, K.; Sun, H.; Yin, S. One-Step Synthesis of Single-Layer MnO 2 Nanosheets with Multi-Role Sodium Dodecyl Sulfate for High-Performance Pseudocapacitors. *Small* **2015**, *11*, 2182−2191.

(21) Wang, Y.; Feng, X.; Villalobos, M.; Tan, W.; Liu, F. Sorption Behavior of Heavy Metals on Birnessite: Relationship with Its Mn Average Oxidation State and Implications for Types of Sorption Sites. *Chem. Geol.* **2012**, *292*−*293*, 25−34.

(22) Ling, F. T.; Post, J. E.; Heaney, P. J.; Ilton, E. S. The Relationship between Mn Oxidation State and Structure in Triclinic and Hexagonal Birnessites. *Chem. Geol.* **2018**, *479*, 216−227.

(23) Ferreira, C. M. H.; Pinto, I. S. S.; Soares, E. V.; Soares, H. M. V. M. (Un)Suitability of the Use of PH Buffers in Biological, Biochemical and Environmental Studies and Their Interaction with Metal Ions-a Review. *RSC Adv.* **2015**, *5*, 30989−31003.

(24) Baltrusaitis, J.; Schuttlefield, J. D.; Zeitler, E.; Jensen, J. H.; Grassian, V. H. Surface Reactions of Carbon Dioxide at the Adsorbed Water-Oxide Interface. *J. Phys. Chem. C* **2007**, *111*, 14870−14880.

(25) Baltrusaitis, J.; Schuttlefield, J.; Zeitler, E.; Grassian, V. H. Carbon Dioxide Adsorption on Oxide Nanoparticle Surfaces. *Chem. Eng. J.* **2011**, *170*, 471−481.

(26) McKenzie, R. M. The Synthesis of Birnessite, Cryptomelane, and Some Other Oxides and Hydroxides of Manganese. *Mineral. Mag.* **1971**, *38*, 493−502.

(27) Loya, A.; Stair, J. L.; Ren, G. Simulation and Experimental Study of Rheological Properties of CeO2−Water Nanofluid. *Int. Nano Lett.* **2015**, *5*, 1−7.

(28) Qiu, H.; Lv, L.; Pan, B. C.; Zhang, Q. J.; Zhang, W. M.; Zhang, Q. X. Critical Review in Adsorption Kinetic Models. *J. Zhejiang Univ., Sci., A* **2009**, *10*, 716−724.

(29) Zou, W.; Zhang, J.; Li, K.; Han, P.; Han, R. Characterization of Manganese Oxide and the Adsorption of Copper(II) and Lead(II) Ions from Aqueous Solutions. *Adsorpt. Sci. Technol.* **2009**, *27*, 549−565.

(30) Azizian, S. Kinetic Models of Sorption: A Theoretical Analysis. *J. Colloid Interface Sci.* **2004**, *276*, 47−52.

(31) Zhou, X.; Zhou, X. The Unit Problem in the Thermodynamic Calculation of Adsorption Using the Langmuir Equation. *Chem. Eng. Commun.* **2014**, *201*, 1459−1467.

https://dx.doi.org/10.1021/acsomega.0c05069
ACS Omega 2020, 5, 32697−32705